Journal of Materials Chemistry A

ROYAL SOCIETY OF CHEMISTRY

PAPER

View Article Online
View Journal | View Issue

Cite this: J. Mater. Chem. A, 2024, 12, 21997

Porous metal microsphere M@C-rGO (metal = Mn, Fe, Co, Ni, Cu) aerogels with high low-frequency microwave absorption, strong thermal insulation and superior anticorrosion performance†

Junfeng Qiu,[a] Xin Liu,[a] Chunyi Peng,[a] Sihan Wang,[a] Rongchen Wang[a] and Wei Wang *[ab]

Nowadays, the development of multifunctional electromagnetic wave absorbers to improve the survivability of military equipment in complex environments is becoming a significant and unavoidable challenge. Here, three-dimensional porous metal microsphere@chitosan reduced graphene oxide (M@C-rGO, M = Mn, Fe, Co, Ni, Cu) aerogels are constructed *via* a simple ice template method and subsequent pyrolysis. The embedding of different metal microspheres realizes the modulation of the electromagnetic parameters of the synthesized aerogel, achieving a balance between attenuation capability and impedance matching. As expected, the synthesized Cu@C-rGO aerogel exhibits strong microwave absorption in the C-band with a minimum reflection loss (RL_{min}) of −59.28 dB, which also features an effective absorption bandwidth (EAB) of 6.32 GHz in the high-frequency band. Furthermore, the synthesized aerogels have superior radar stealth, thermal insulation and anticorrosion properties. Typically, the thermal conductivity of Cu@C-rGO is 0.0339 W m^{-1} K^{-1}, and the charge transfer resistance (R_{ct}) is 1.421 × 10^5 Ω cm^2. Impressively, more than 90% of the EAB could be retained after 7 days of corrosion in NaCl solution. Consequently, this work provides valuable guidance and insight into the development of multifunctional electromagnetic wave absorbers.

Received 12th June 2024
Accepted 10th July 2024

DOI: 10.1039/d4ta04051a

rsc.li/materials-a

1. Introduction

With the rapid development of fifth-generation (5G) wireless technology, electronic devices and artificial intelligence technology have brought great convenience to our lives, but have also caused serious problems of electromagnetic radiation and electromagnetic pollution.[1–3] Developing efficient microwave absorbers is an effective way to reduce and eliminate electromagnetic wave radiation.[4–7] In contrast to traditional high-frequency radar signals, 5G wireless signals are mainly located in the C-band and lower frequencies.[8–11] However, the absorption frequencies of most current microwave absorbers are concentrated in the high-frequency range (X and Ku bands).[12,13] Therefore, it is urgent to develop microwave absorption materials with strong absorption in low-frequency bands.

High magnetic loss has been considered as one of the critical factors for obtaining strong absorption at low-frequencies in microwave absorption materials.[14–16] Magnetic materials represented by Fe, Co and Ni and their alloys have attracted much attention in the field of microwave absorption due to their high saturation magnetization strength and excellent magnetic loss performance.[17,18] However, due to the lack of dielectric loss, a single magnetic metal is usually inadequate to obtain excellent microwave absorption performance owing to impedance mismatch.[19] To realize the effective matching of complex permittivity and complex permeability, many scholars have researched on composites of magnetic metals and light dielectric materials such as carbon materials. Che *et al.* synthesized FeCo@C hollow microspheres through a confined diffusion strategy, obtaining a minimum reflection loss (RL_{min}) of −35.9 dB and an effective absorption bandwidth (EAB) covering almost the entire C-band.[20] Also, Liu *et al.* synthesized size-tunable Co/CoO nanoparticles by disassembling the cubic zeolitic imidazolate framework (ZIF-67) and subsequent hydrogen reduction, which resulted in an RL_{min} of −90.3 dB at 4.4 GHz.[19] Jiang *et al.* constructed MXene/CoNi/N-CNT three-dimensional (3D) heterostructures by electrostatic assembly, which exhibited an RL_{min} value of −52.64 dB at 3.12 GHz.[14]

Recently, achieving multifunctional applications has been an important research direction of advanced materials. However, magnetic metals usually suffer from disadvantages

[a]Department of Physics and Electronics, School of Mathematics and Physics, Beijing University of Chemical Technology, Beijing 100029, China. E-mail: wangwei@mail.buct.edu.cn

[b]Beijing Key Laboratory of Environmentally Harmful Chemical Analysis, Beijing University of Chemical Technology, Beijing 100029, China

† Electronic supplementary information (ESI) available. See DOI: https://doi.org/10.1039/d4ta04051a

such as high density, poor dispersibility and susceptibility to corrosion, which seriously restrict their multifunctional applications. Graphitic carbon is considered to be a perfect atom-scale barrier that prolongs the path of penetration of corrosive media (*e.g.*, H_2O, O_2 and Cl^-) into the metal substrate, due to its impermeability and chemical stability.[18] As a typical two-dimensional carbon material, reduced graphene oxide (rGO) with low density, high specific surface area, abundant surface defects, and strong conductive loss has become a representative candidate for high-performance microwave absorption materials.[21,22] However, the impedance mismatch and skinning effect caused by the high conductivity of rGO hinder its further development in the field of microwave absorption. In fact, combining rGO with magnetic metals can balance the impedance matching and attenuation ability to enhance the microwave absorption performance of the materials. Meanwhile, rGO can also provide an anticorrosion barrier to improve the long-term stability of the material in a corrosive environment. For instance, Xu *et al.* synthesized a three-dimensional NiAl layered double hydroxide/graphene (NiAl-LDH/G) composite as an anticorrosion microwave absorber with an RL_{min} of −41.5 dB and an EAB of 4.4 GHz by atomic layer deposition. Remarkably, the composite exhibits long-term corrosion resistance due to the synergetic effect of the superior impermeability of graphene and the chloridion-capture capacity of the NiAl-LDH.[23] Yao *et al.* applied the rare earth lanthanum (La) pinning effect to FeCo/rGO composites to achieve a corrosion-resistant and highly efficient microwave absorber. As a result, the FeCo@rGO composites exhibit excellent microwave absorption properties covering a frequency range of 6.11 GHz at 1.55 mm. Meanwhile, the electromagnetic properties of the absorber remained stable even after prolonged exposure to 3.5 wt% NaCl solution for at least 15 days.[24] In addition, the unique two-dimensional structure of rGO enables its excellent energy storage and thermal management capabilities.[25,26] Thus, rational component modulation and innovative structural design are key to the development of multifunctional composites.

Since the intrinsic mechanism and parametric conditions of low-frequency microwave absorption are still unclear enough, this study tries to find out the parametric conditions of low-frequency microwave absorption using numerical simulation. Subsequently, magnetic and nonmagnetic metal microspheres were embedded into chitosan-rGO aerogels by a simple ice template method and pyrolysis to modulate the complex permittivity and magnetic permeability of the absorber. Remarkably, the as-obtained composites exhibit strong absorption at low-frequency and a wide effective absorption bandwidth in the high-frequency band, based on excellent dielectric loss and good impedance matching. Furthermore, the composite aerogels exhibit excellent thermal insulation and anticorrosion capabilities due to the unique 3D porous structure. Therefore, this work provides theoretical and experimental guidance for the preparation of multifunctional materials for low-frequency microwave absorption with strong thermal insulation and excellent anticorrosion performance.

2. Experimental section

2.1. Materials

Sulfuric acid (H_2SO_4), phosphoric acid (H_3PO_4), hydrogen peroxide (H_2O_2), potassium permanganate ($KMnO_4$), graphite powder (325 mesh), manganese chloride tetrahydrate ($MnCl_2 \cdot 4H_2O$), ferric chloride hexahydrate ($FeCl_3 \cdot 6H_2O$), cobalt chloride hexahydrate ($CoCl_2 \cdot 6H_2O$), nickel chloride hexahydrate ($NiCl_2 \cdot 6H_2O$), copper sulfate pentahydrate ($CuSO_4 \cdot 5H_2O$), glacial acetic acid, glucose, chitosan, urea paraffin and ethanol were directly used after purchase from Sinopharm Chemical Reagent Co., Ltd, China without further purification. Graphene oxide was synthesized according to the modified Hummers' method.

2.2. Synthesis of the metal microsphere precursor

Firstly, 0.01 mol of metal ion, 0.015 mol glucose and 0.02 mol urea were dissolved into 60 mL deionized water. After ultrasonic treatment for 30 min, the resulting mixture was transferred into a 100 mL Teflon-lined stainless-steel autoclave, and heated at 180 °C for 20 h. The obtained black precipitate was washed three times with water and ethanol, and then, oven-dried overnight at 60 °C to obtain the precursor. Here, the obtained samples are denoted as Mn–P, Fe–P, Co–P, Ni–P and Cu–P according to the added metal salts, $MnCl_2 \cdot 4H_2O$, $FeCl_3 \cdot 6H_2O$, $CoCl_2 \cdot 6H_2O$, $NiCl_2 \cdot 6H_2O$, and $CuSO_4 \cdot 5H_2O$, respectively.

2.3. Synthesis of M@C-rGO aerogels

0.1 g of metal precursor, 50 mg of GO and 0.2 g of chitosan were added to 15 mL of deionized water and sonicated for 1 h to form a homogeneous suspension. After that, 0.4 mL of glacial acetic acid was quickly dripped to form a gel. Then, the gel was poured into molds and freeze-dried at −50 °C for 48 h. Finally, M@C-rGO aerogels were obtained after 500 °C calcination for 90 min under a nitrogen atmosphere. The synthesized aerogels were named Mn@C-rGO, Fe@C-rGO, Co@C-rGO, Ni@C-rGO and Cu@C-rGO according to the metal microsphere precursors. Similarly, all steps were repeated without the metal sphere precursor to obtain the sample C-rGO.

2.4. Characterization

The morphology of the samples was characterized using a scanning electron microscope (SEM, Hitachi S-3500N). The crystal structure and crystallinity of the samples were analyzed with an XRD-6000 diffractometer using Cu Kα radiation at a scanning rate of 5° min^{-1}. Raman spectra at room temperature were recorded using a LabRAM ARAMIS spectrometer (HORIBA Jobin-Yvon) with an excitation of 532 nm. The bonding characteristics and chemical composition of the samples were studied with a PHI Quantera II XPS Scanning Microprobe. The infrared images were taken with a thermographic camera (HM-TPK20-3AQF/W) and the thermal conductivity was measured using a thermal constant analyzer (Hot-Disk TPS2200).

2.5. Electromagnetic wave absorption measurements

First, the as-synthesized aerogels and paraffin with a mass ratio of 2 : 8 were added into 4 mL of hexane solution. Then, the as-obtained mixture was sonicated for 30 min until a homogeneous solution formed, and then the mixed solution was dried at 60 °C overnight. The as-formed black waxy solid was placed in a metal mold and pressed as a hollow cylinder with outer and inner diameters of 7.0 mm and 3.04 mm, respectively. Subsequently, the electromagnetic performance and S parameters of the samples were characterized using a vector network analyzer (VNA, Agilent E8362B) using the coaxial-line method in the frequency range of 2–18 GHz.

2.6. Anticorrosion performance measurements

The corrosion resistance of the samples was measured using the classical three-electrode system of an electrochemical workstation (CHI660E). The platinum sheet electrode, Ag/AgCl electrode and glassy carbon electrode were used as the counter electrode, reference electrode and working electrode respectively. The open-circuit potential (OCP), linear sweep voltammetry (LSV) curves and electrochemical impedance spectroscopy (EIS) spectra of the samples were recorded under acidic (0.5 M H_2SO_4), neutral (3.5 wt% NaCl) and alkaline (1.0 M NaOH) conditions. To prepare the working electrode, 3 mg of sample was mixed with 510 μL of solvent (5 wt% Nafion, isopropanol and deionized water in the ratio of 1 : 20 : 30) and sonicated for 1 h to obtain a homogeneous suspension. 10 μL of the above suspension was dropped onto a glassy carbon electrode with a radius of 2.5 mm and dried at room temperature. The LSV curve is measured at a scan rate of 1 mV s^{-1} with a voltage range of OCP ± 0.6 V. EIS was performed in the 10^5–10^{-2} Hz range and fitted with ZView software.

2.7. Radar cross-section (RCS) simulation

The RCS values of the samples were simulated using a CST Studio Suite 2020. The simulation model was a double-layered square (100 × 100 mm) with a wave-absorbing layer of 4 mm thickness in the upper layer and a (perfect electric conductor) PEC layer of 5 mm thickness in the lower layer. And then, the simulation model was placed in the *X*–*O*–*Y* plane, with the electromagnetic wave in the linear polarization plane incident along the negative direction of the *z*-axis, and the electric polarization direction incident along the *x*-axis. Furthermore, open boundary conditions are applied in all directions and the electromagnetic wave frequency is set to 7 GHz.

3. Results and discussion

3.1. Numerical simulation

Now, we propose a numerical simulation method to reveal the effect of the change in complex permittivity and complex permeability on the low-frequency microwave absorption performance of the absorbers. Normally, the microwave absorption performance of an absorber is evaluated by the reflection loss (RL) value. According to the transmission line theory, the RL of a material is closely related to its complex permittivity ($\varepsilon_r = \varepsilon' - j\varepsilon''$) and complex permeability ($\mu_r = \mu' - j\mu''$),[27,28] where the real and imaginary parts of the electromagnetic parameters are related to the storing and attenuating ability of electromagnetic wave energy, respectively.[29] Meanwhile, the dielectric loss tangent ($\tan\delta_\varepsilon = \varepsilon''/\varepsilon'$) and magnetic loss tangent ($\tan\delta_\mu = \mu''/\mu'$) values reflect the strength of the dielectric loss and magnetic loss, respectively. Furthermore, according to the transmission line theory, the corresponding RL values can be obtained from the following equations:[30]

$$\mathrm{RL(dB)} = 20\lg\left|\frac{Z_{in} - Z_0}{Z_{in} + Z_0}\right| \quad (1)$$

$$Z_{in} = Z_0\sqrt{\left|\frac{\mu_r}{\varepsilon_r}\right|}\tan h\left(j\frac{2\pi fd}{c}\sqrt{\mu_r\varepsilon_r}\right) \quad (2)$$

where Z_{in} corresponds to the normalized input impedance of the absorbers, Z_0 is equivalent to the impedance of free space, and d is the thickness of the absorbers, respectively. So the RL value is directly determined by the five parameters, ε', ε'', μ', μ'' and d. Here, the values of ε', $\varepsilon''/\varepsilon'$, μ', μ''/μ' and d are defined to explore the variation rule of RL to investigate the electromagnetic parameter conditions for low-frequency microwave absorption.

The numerical simulations are divided into the nonmagnetic and magnetic cases. First, for nonmagnetic materials, μ' and μ'' are defined as 1 and 0, respectively. After reviewing the dielectric constants of an abundance of microwave-absorbing materials, ε' is defined from 4 to 12 (interval of 2), $\varepsilon''/\varepsilon'$ is defined from 0.2 to 0.8 (interval of 0.2), and the thickness is fixed from 2 to 5 mm (interval of 0.5 mm). In Fig. S1,† when the thickness and ε'' are fixed, the matching frequency of the RL peak is related to ε', *i.e.*, as ε' increases, the RL peak shifts to a lower frequency. At the same time, when the ε' increases it also leads to a slow shift of the RL peak towards lower frequency. In addition, $\varepsilon''/\varepsilon'$ affects the magnitude of the RL value, and a smaller $\varepsilon''/\varepsilon'$ yields a smaller RL value when the ε' increases. The variation of the RL peak corresponding to the frequency (RL_{min}@Frequency) with the complex dielectric constant can be clearly seen in Fig. S3a.† It can be seen that the RL_{min}@-Frequency moves to lower frequencies as ε' increases. Therefore, for non-magnetic materials, an increase in ε' and an appropriate decrease in $\varepsilon''/\varepsilon'$ are required to achieve strong absorption at low frequencies.

Similarly, for a magnetic absorber, ε' and $\varepsilon''/\varepsilon'$ are defined as 6 and 0.4, while μ' is defined from 1 to 4 (interval of 1), μ''/μ' is defined from 0.2 to 0.8 (interval of 0.2), and the thickness is fixed from 2 to 5 mm (interval of 0.5 mm). As in Fig. S2,† the RL_{min}@Frequency moves to a lower frequency with increasing μ', while μ''/μ' determines the magnitude of RL value. It is worth noting that an increase in μ' and μ''/μ' also significantly lead to an increase of EAB, which can cover 2–18 GHz at its maximum. As shown in Fig. S3b,† It is clearly observed that as both μ' and μ'' increase, RL peaks shift to lower frequency, and the shift with increasing μ' is more pronounced. Therefore, for magnetic absorbers, larger μ' and μ'' not only favor the shift of RL to a lower frequency, but also result in a wider EAB.

Moreover, the RL peak of the absorber also shifts to a lower frequency with increasing thickness, which can be explained by the quarter-wavelength model as follows:[31,32]

$$f_m = \frac{nc}{4t_m\sqrt{|\varepsilon_r\mu_r|}}(n = 1, 3, 5\ldots) \quad (3)$$

where t_m is the matching thickness and f_m is the absorption peak frequency. Seen from eqn (3), f_m decreases with increasing ε_r and μ_r at a certain t_m, which is consistent with the results of the previous numerical simulations. However, it is worth noting that an excessively high ε_r may inhibit the microwave absorption performance due to impedance mismatch.

In summary, there are two ways to achieve low-frequency absorption: (1) sufficiently large ε' and small $\varepsilon''/\varepsilon'$ values; (2) introduction of strong magnetic losses. So, in our experiments, the rGO aerogel with high electrical conductivity is selected as the substrate to provide the ε' values. Furthermore, classical magnetic metals (Fe, Co, and Ni) and their neighboring nonmagnetic metals (Mn and Cu) are introduced to introduce magnetic losses or reduced $\varepsilon''/\varepsilon'$ values to achieve strong absorption at low frequency.

3.2. Multifunctional M@C-rGO aerogels

3.2.1. Morphology and structural characterization. The synthesis of M@C-rGO aerogels is illustrated in Fig. 1a. First, metal ions, glucose and urea form microspheres owing to a complexation reaction during the hydrothermal process. The surface of the metal microsphere precursor is smooth with a diameter of about 5 μm as shown in Fig. S4a.† Here, the group VIII metal ions Fe^{3+}, Co^{2+}, Ni^{2+} and their neighboring Mn^{2+} and Cu^{2+} are selected to prepare the metal precursors by the same synthetic route. Subsequently, due to the protonation of free amino groups on the chains of the chitosan molecule, chitosan can be solubilized in an acetic acid solution to form a homogeneous hydrogel precursor. Meanwhile, the amino group can achieve *in situ* N-doping of the aerogels in the subsequent carbonization process without the need of an additional nitrogen source. The inter-crosslinked rGO nanosheets will form a unique 3D porous structure as in Fig. S4b and c,† which provides attachment sites for the metal microspheres. As shown in Fig. 1b–f, the diameters of the metal microspheres are reduced to about 3–4 μm after calcination. Moreover, after cross-linking by chitosan, the rGO nanosheets are wrapped around the surface of the metal microspheres. Additionally, the elemental mapping images of samples distinctly manifest the distribution of C, O and corresponding metal elements in the as-prepared M@C-rGO aerogels. In fact, M@C-rGO aerogels with a low density of about 35 mg cm^{-3} can be placed on a leaf as in Fig. S5 and S6.†

The phase and crystal structure of the samples are determined by X-ray diffraction (XRD) as shown in Fig. 2a. It is clearly observed that the wide peaks around 25° in all samples belong to the (002) crystal plane of rGO, indicating that GO is reduced to rGO in the calcination.[33] Similarly, the metal sphere precursors Co–P, Ni–P and Cu–P are reduced to Co, Ni and Cu, respectively. In particular, the temperatures do not reach the reduction temperatures of Fe and Mn, thus the XRD patterns of Mn@C-rGO and Fe@C-rGO have peaks of Fe_3O_4 and MnO.[4,34] Moreover, X-ray photoelectron spectroscopy (XPS) analysis of the samples can further reveal their chemical composition and elemental valence states. In Fig. 2b, the XPS survey spectrum of sample C-rGO has only peaks for C 1s, N 1s and O 1s, while the peaks of Mn 2p, Fe 2p, Co 2p, Ni 2p and Cu 2p are also observed for the M@C-rGO aerogels with the addition of the corresponding metal microspheres. Specifically, the high-resolution spectrum of C 1s as in Fig. S7a† can be fitted to four characteristic peaks 284.7, 285.3, 286.2 and 288.5 eV belonging to C–C/C=C, C–N, C–O and C=O bonds, respectively.[34,35] Here, chitosan is rich in nitrogen, and the doped nitrogen atoms exist in the form of pyridine N (398.7 eV), pyrrole N (400.5 eV) and graphite N (403.4 eV) as shown in Fig. S7b.[36,37]† The difference in electronegativity between carbon and nitrogen atoms alters the distribution of the electron clouds, which promotes the generation and vibration of electric dipoles. This helps to induce dipole polarization and contributes to the attenuation of electromagnetic waves.[4] In the O 1s high-resolution spectrum of C-rGO (Fig. S7c†), the peaks at 532.2 eV and 532.5 eV belong to C–O bonds and oxygen in adsorbed water, respectively.[38] Noteworthily, after loading the metal microspheres, the synthesized M@C-rGO aerogels show an obvious peak of metal–oxygen at about 530.3 eV.[39] Furthermore, as shown in Fig. S8,† $2p_{2/3}$ and $2p_{2/1}$ of the metals Mn, Fe, Co, Ni, and Cu are clearly observed, indicating the successful loading of the metal microspheres.

Besides, the degree of graphitization of the composites is characterized by the Raman spectrum. The characteristic band at ~1350 cm^{-1} (D-band) is attributed to disordered carbon, while the band at ~1590 cm^{-1} (G-band) belongs to the in-plane stretching vibration of sp^2 hybrid carbon atoms.[29,40] Thus, the intensity ratio between the D-band and G-band (I_D/I_G) can reveal the degree of graphitization of the material.[41] As illustrated in Fig. 2c, the I_D/I_G of the C-rGO aerogel is only 0.928, while those of Mn@C-rGO, Fe@C-rGO, Co@C-rGO, Ni@C-rGO and Cu@C-rGO aerogels are 0.966, 0.954, 0.980, 0.976 and 0.942, respectively. It is clear that the loading of metal microspheres introduces more defects into the M@C-rGO aerogels and decreases the degree of graphitization of the carbon material. The decrease in graphitization decreases the electrical conductivity of the composites leading to a lower ε'', while the increase in defects results in more dipole polarization loss to the samples. Furthermore, different metal microspheres are crucial for modulating the magnetic properties of M@C-rGO aerogels.

Theoretically, μ_r is closely related to the saturation magnetization (M_s) strength and coercivity (H_c) which can be expressed as follows:[42]

$$\mu_r = \frac{\mu}{\mu_0} = \frac{{M_s}^2}{\mu_0(akH_cM_s + b\lambda\xi)} \quad (4)$$

where a and b are constants determined by the material composition, k, λ and ξ are the proportional coefficient, magnetostrictive coefficient and elastic strain parameter, respectively. From the above equations, a large M_s and a small H_c render the material a larger permeability, which further

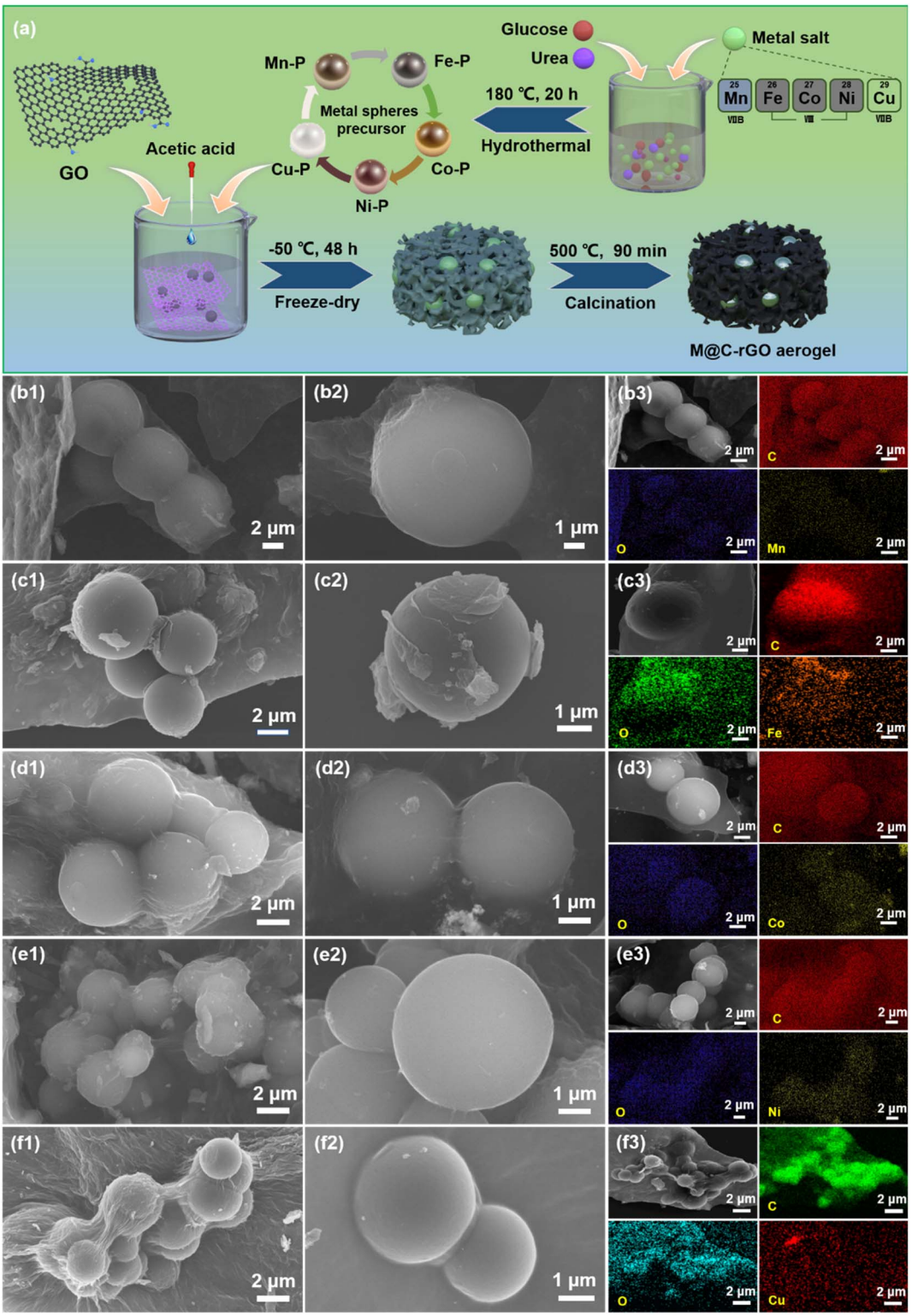

Fig. 1 (a) The schematic illustration of the synthetic process of M@C-rGO aerogels. The SEM images and EDS elemental mapping of (b) Mn@C-rGO, (c) Fe@C-rGO, (d) Co@C-rGO, (e) Ni@C-rGO and (f) Cu@C-rGO.

enhances the magnetic loss under the alternating electromagnetic field. The hysteresis loops of the samples (Fig. 2d) show that the Fe@C-rGO, Co@C-rGO and Ni@C-rGO aerogels have strong magnetic properties with the M_s of 15.2, 14.6 and 2.1 emu g^{-1}, respectively. Meanwhile, the H_c of Fe@C-rGO, Co@C-rGO and Ni@C-rGO aerogels are 252.4, 301.3 and 10.8 Oe. In contrast, Mn@C-rGO and Cu@C-rGO aerogels show negligible magnetic and antimagnetic properties. Therefore, Fe@C-rGO

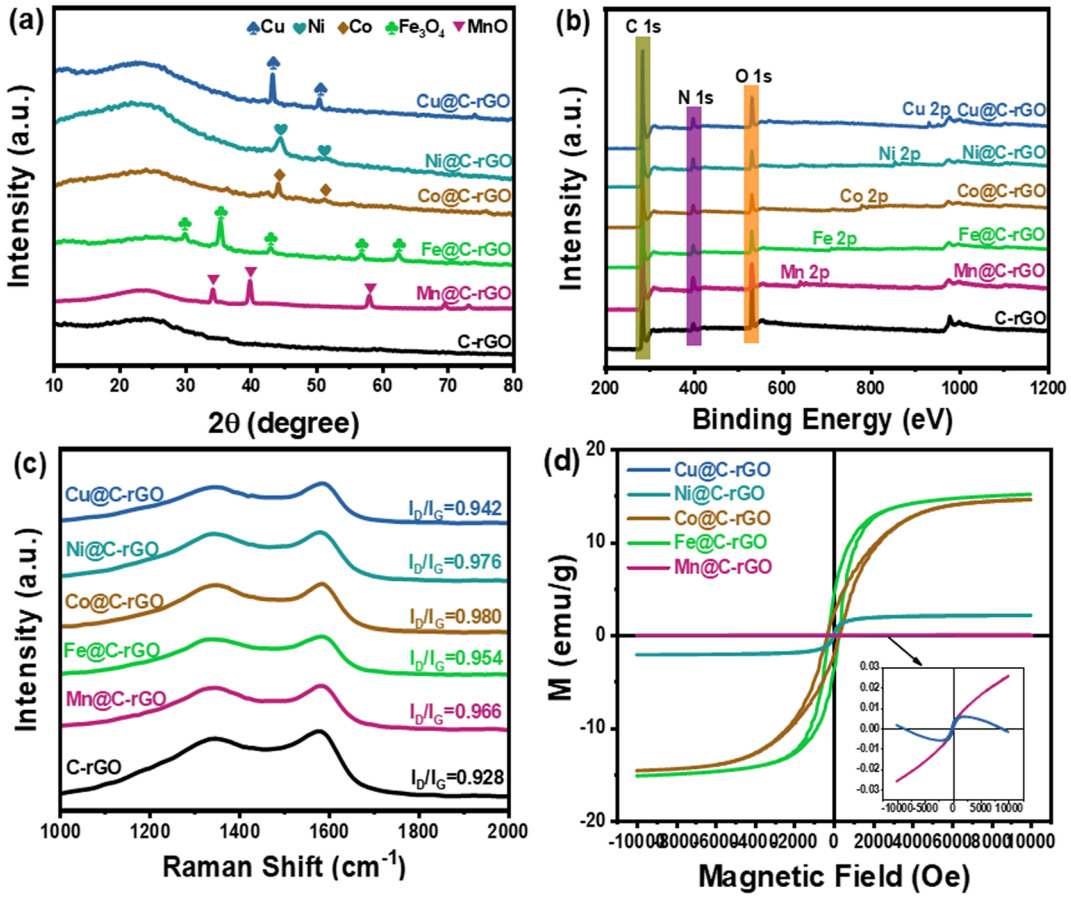

Fig. 2 Compositional characterization: (a) the XRD patterns, (b) XPS survey spectra, (c) Raman spectra and (d) the hysteresis loop of the samples.

and Co@C-rGO are expected to demonstrate stronger magnetic losses and contrast with the other samples, which correspond to the two ways of realizing low-frequency microwave absorption in the previous numerical simulations.

3.2.2. Microwave absorption performance of M@C-rGO aerogels. Typically, when RL <−10 dB, it means that 90% of the incident electromagnetic wave will be absorbed by the absorber, and the corresponding frequency band is defined as the effective absorption band.[43,44] Clearly, Fig. 3a–f show the microwave absorption performance for M@C-rGO aerogels with a filling ratio of 20 wt%. Notably, C-rGO exhibits excellent microwave absorption performance in the high-frequency band with an RL_{min} of 31.98 dB at 14.4 GHz and an EAB of 6.16 GHz (11.84–18 GHz). Nevertheless, Fe@C-rGO and Co@C-rGO exhibit negligible microwave absorption performance with RL_{min} values of only −10.43 and 9.7 dB, respectively. Surprisingly, Mn@C-rGO, Ni@C-rGO, and Cu@C-rGO show strong microwave absorption in the C-band with RL_{min} values up to −53.42, −53.64, and −59.28 dB at thicknesses of 4.6, 4.1, and 4.00 mm, respectively. Moreover, the composites also exhibit wide absorption bandwidths in the high-frequency band, with EAB up to 6.16, 6.64, and 6.32 GHz at thicknesses of 2.50, 2.55, and 2.38 mm, respectively, which completely cover the Ku-band. Obviously, as shown in Fig. 3g–i, Mn@C-rGO, Ni@C-rGO, and Cu@C-rGO exhibit excellent microwave absorption properties with strong absorption at low-frequency and broad bandwidth at high-frequency, and are highly promising microwave absorption materials.

The microwave absorption properties of the synthesized aerogels and other rGO-based absorbers were further analyzed and compared as shown in Fig. 4 and Table S1.† Mn@C-rGO, Ni@C-rGO, and Cu@C-rGO exhibit a wide EAB of 6.16, 6.64 and 6.32 GHz, respectively, outperforming most of the rGO-based absorbers. Furthermore, Mn@C-rGO, Ni@C-rGO, and Cu@C-rGO show strong microwave absorption (RL_{min} = −53.42, −53.64 and −59.28 dB) in the lower frequency bands of 6.88, 7.92 and 7.6 GHz with thicknesses of 4.60, 4.10, and 4.00 mm, respectively. In fact, an absorber with a wide bandwidth and a strong absorption capacity has a huge potential for applications. Thus, the synthesized aerogels can be among the advanced microwave absorbers.

It is well known that the real (ε') and imaginary (ε'') parts of the complex dielectric constant reflect the storage and loss ability of electrical energy, respectively.[45] As seen from Fig. 5a and b, the decreasing trend of the permittivity with increasing frequency for all samples is due to the dispersion effect, which is caused by the fact that the orientation of the electric dipole lags behind the periodical variation of the electromagnetic field.[29] In particular, C-rGO shows the highest ε' value decreasing from 12.03 to 5.53 due to the higher conductivity of

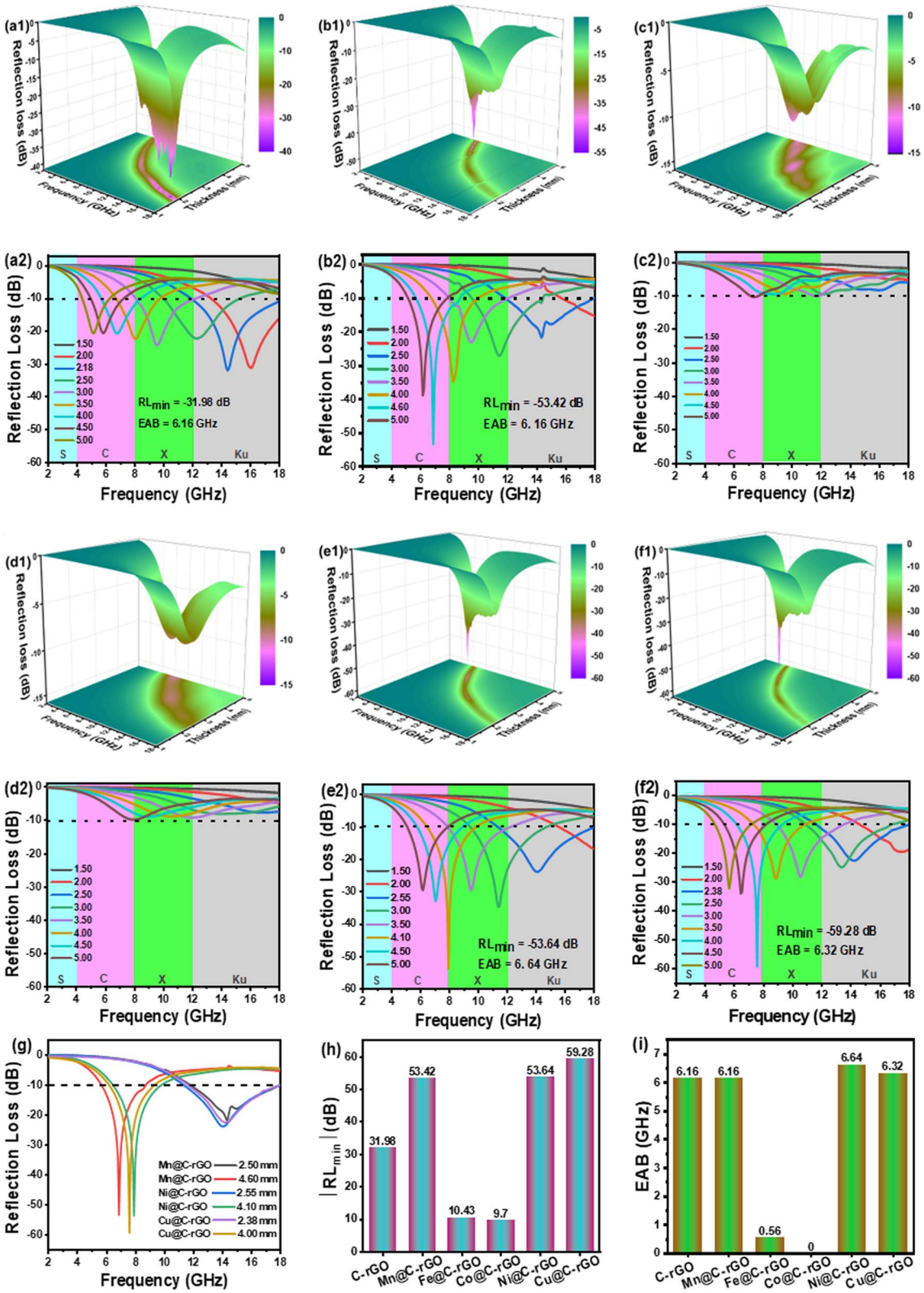

Fig. 3 The 3D RL contour plots and RL values of (a) C-rGO, (b) Mn@C-rGO, (c) Fe@C-rGO, (d) Co@C-rGO, (e) Ni@C-rGO and (f) Cu@C-rGO. The comparison of (g) RL values, (h) RL_{min} and (i) EAB for samples.

the carbon material. Then, with the addition of metal microspheres, the complex permittivity of M@C-rGO aerogels decreases to different degrees in both the real and imaginary parts. In detail, the values of ε' decrease from 8.80 to 4.42, 6.06 to 4.05, 5.50 to 3.50, 9.41 to 4.46 and 9.62 to 4.87 for the Mn@C-rGO, Fe@C-rGO, Co@C-rGO, Ni@C-rGO and Cu@C-rGO,

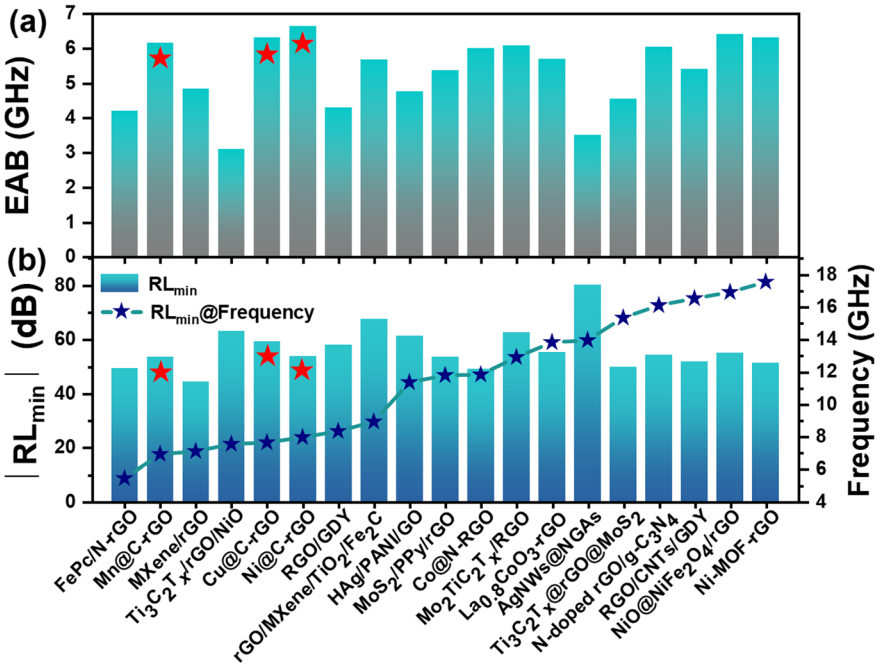

Fig. 4 Comparison of microwave absorption properties: (a) EAB and (b) RL_{min} *versus f* of reported graphene-based absorbers.

respectively. Similarly, a decrease of ε'' could be observed with the increase in the frequency in the range of 3.40–1.80, 1.66–0.80, 1.77–0.76, 4.11–2.01 and 3.03–2.06 for the five samples, respectively. Furthermore, the tangent of permittivity ($\tan\delta_\varepsilon = \varepsilon''/\varepsilon'$) can further reveal the dielectric loss properties of the material. As shown in Fig. 5c, the $\tan\delta_\varepsilon$ values of the samples exhibit similar variations in the order of C-rGO > Ni@C-rGO > Cu@C-rGO > Mn@C-rGO > Co@C-rGO > Fe@C-rGO. According to the previous numerical simulations, C-rGO with the maximum ε' favors the shift of the RL peak to a lower frequency, but the larger $\varepsilon''/\varepsilon'$ prevents it from achieving strong microwave absorption at lower frequency. Obviously, the composite of metal microspheres can effectively modulate the dielectric constant of the synthesized aerogel. In particular, Cu@C-rGO maintains a large ε' along with a small $\varepsilon''/\varepsilon'$, thus it exhibits a minimum RL_{min} at the C-band, which is in accordance with the results of the above numerical simulations for nonmagnetic materials.

In addition, the Cole–Cole curve can describe the relationship between the real and imaginary parts of the complex permittivity. According to the Debye theory, the complex permittivity can be expressed by the following equations:[46]

$$\left(\varepsilon' - \frac{\varepsilon_s - \varepsilon_\infty}{2}\right)^2 + \left(\varepsilon''\right)^2 = \left(\frac{\varepsilon_s - \varepsilon_\infty}{2}\right)^2 \quad (5)$$

where ε_s is the static dielectric constant, τ is the polarization relaxation time, ε_0 (8.85×10^{-12} F m^{-1}) is the permittivity of free space, ε_∞ is the relative permittivity at high-frequency. Generally, a semicircle on the ε'–ε'' curve corresponds to a Debye relaxation process.[47,48] In Fig. S9,† more than two semicircles can be clearly observed on the Cole–Cole curves of the samples, which implies the existence of multiple polarization relaxation processes in the material, such as dipolar polarization and interfacial polarization.[49] Here, the residual functional groups and doped N atoms on the rGO nanosheets form polarization centers that induce the generation of dipole polarization.[26,37] In addition, the addition of metal microspheres generates more defects in the composites, which also induces dipole polarization in the alternating electromagnetic field. Furthermore, the abundant non-homogeneous interfaces between the metal microspheres and the carbon material result in space charge aggregation forming capacitor-like structures. Subsequently, the unevenly accumulated charges at the contact surfaces are forced to rearrange along the direction of the high-frequency electric field, leading to strong interfacial polarization relaxation loss.

As shown in Fig. 5d and e, the real part (μ') and imaginary part (μ'') of the magnetic permeability are close to 1 and 0, respectively. Moreover, as presented in Fig. 5c and f, the dielectric loss is higher than the magnetic loss for all samples, indicating that the dielectric loss is the dominant factor in the microwave absorption of electromagnetic waves. Generally, the magnetic loss of an absorber is mainly due to hysteresis loss, domain wall resonance, eddy current loss, natural resonance and exchange resonance. Meanwhile, the domain wall resonance and hysteresis loss can be neglected at the frequency range of 2.0–18.0 GHz.[46] Herein, the C_0 curve, defined as $C_0 = \mu''(\mu')^{-2}f^{-1}$, can be analyzed for the contribution of eddy current losses to the magnetic loss.[38] If C_0 is constant at different frequencies, the magnetic loss of the absorber is dominated by eddy current loss.[8,50] Fig. 5g shows the C_0–f curve, where a significant fluctuation of C_0 within 2–8 GHz can be observed, indicating that the magnetic loss mainly results from the natural resonance. Simultaneously, C_0 remains constant from

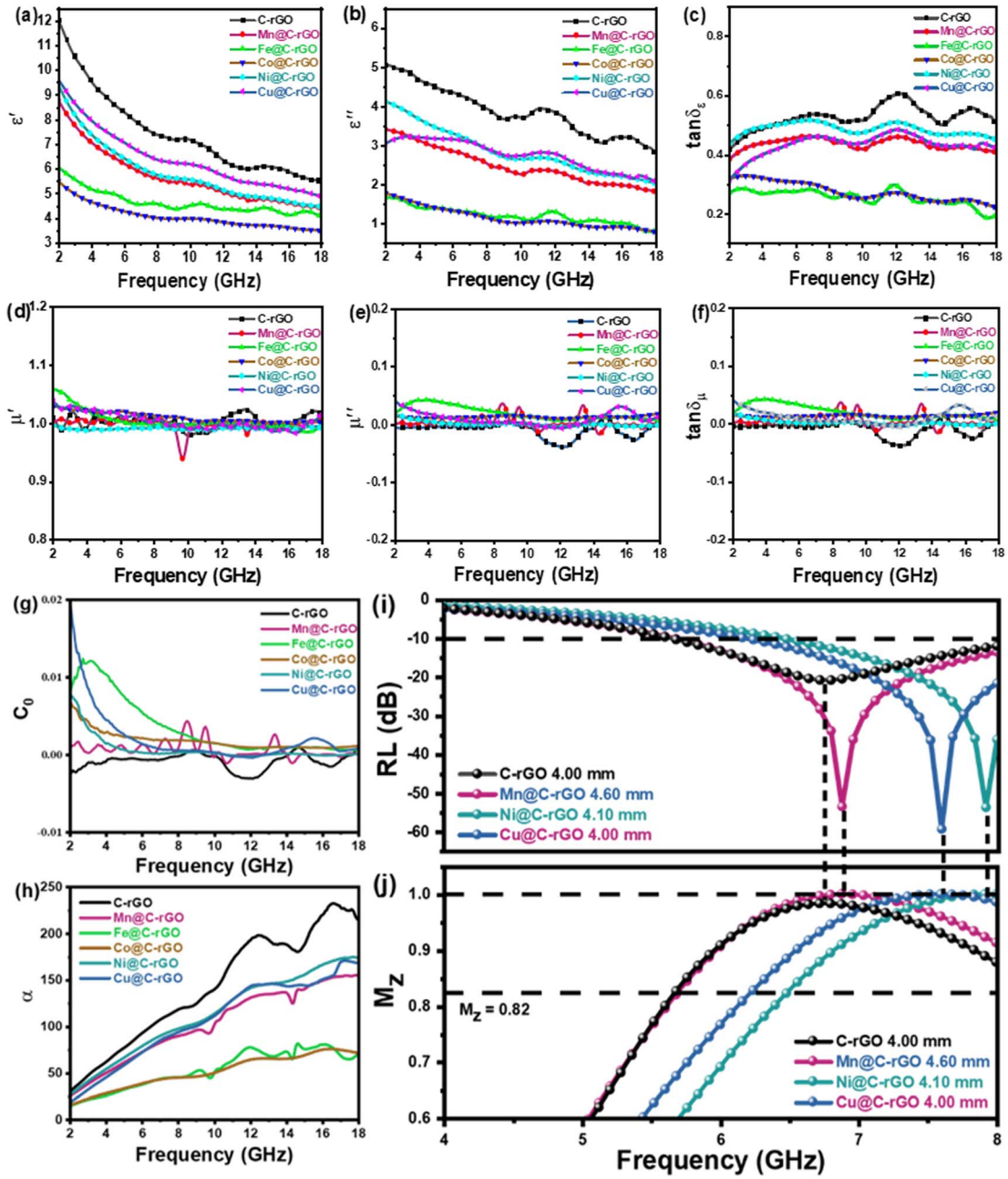

Fig. 5 (a, and b) The complex permittivity, (c, and d) the complex permeability, (e) dielectric loss, and (f) magnetic loss of samples. (g) The eddy current loss coefficient and (h) the attenuation constant. (i) The RL_{min} and corresponding (j) M_Z values for C-rGO, Mn@C-rGO, Ni@C-rGO and Cu@C-rGO at low-frequency.

10 to 18 GHz, indicating that the magnetic loss is mainly determined by eddy current loss in this frequency range. Here, the natural resonance in the low-frequency band of Fe@C-rGO and Co@C-rGO, which have strong magnetic properties, is more significant compared to the other samples. According to previous numerical simulation results, strong magnetic loss will shift the peak reflection loss towards lower frequencies. However, the magnetic metal microspheres provide negligible magnetic loss to the composite aerogel, which differs significantly from the numerical simulation of the magnetic absorber. Meanwhile, the poorer electrical conductivity of the magnetic metal microspheres also leads to a significant decrease in the ε' value. Therefore, Fe@C-rGO and Co@C-rGO failed to achieve superior low-frequency microwave absorption properties.

Typically, the attenuation constant and the impedance matching coefficient are the key parameters that affect the microwave absorption performance of the absorber. In particular, the attenuation constant reflects the ability of the absorber to attenuate the electromagnetic wave, while the impedance matching determines whether the electromagnetic wave can enter the absorber. Specifically, the impedance matching

coefficient (M_Z) and attenuation constant (α) are calculated using the following equations:[31,51]

$$\alpha = \frac{\sqrt{2}\pi f}{c}\sqrt{(\mu''\varepsilon'' - \mu'\varepsilon') + \sqrt{(\mu''\varepsilon'' - \mu'\varepsilon')^2 + (\mu'\varepsilon'' + \mu''\varepsilon')^2}} \quad (6)$$

$$M_Z = \frac{2Z'_{in}/Z_0}{|Z_{in}/Z_0|^2 + 1} \quad (7)$$

where Z'_{in} is the real part of the input impedance. As shown in Fig. 5h, C-rGO shows the largest attenuation constant, and the attenuation constants of Mn@C-rGO, Ni@C-rGO, and Cu@C-rGO decrease with the addition of metal microspheres. However, C-rGO does not display good microwave absorption performance owing to its poor impedance matching. Here, the impedance matching of the absorber is revealed by the M_Z value, where the closer the M_Z value is to 1 the better impedance matching of the microwave absorber is. Moreover, when M_Z >0.82, the corresponding RL value is lower than −10 dB. Obviously, Mn@C-rGO, Ni@C-rGO, and Cu@C-rGO show excellent impedance matching in the C-band, and the frequency of M_Z = 1 corresponds exactly to RL_{min}, proving that the absorber impedance matching is closely related to the microwave absorption performance, as shown in Fig. 5i, and j. In contrast, although the RL peak of C-rGO is shifted to lower frequencies at the same thickness, it fails to achieve strong microwave absorption due to its poor impedance matching, *i.e.*, most of the electromagnetic wave is reflected at the surface of the absorber. Remarkably, the EABs of C-rGO, Mn@C-rGO, Ni@C-rGO and Cu@C-rGO in the C-band are 2.32, 2.32, 1.52 and 1.76 GHz, respectively. Therefore, regulating the electromagnetic parameters of the material to achieve a balance between the attenuation constant and impedance matching is crucial to obtaining an absorber with superior microwave absorption performance.

Most of the traditional military equipment contains metal components with strong electromagnetic scattering characteristics, which are easily recognized by radar detection. The coating of microwave-absorbing materials on the surface of military equipment can effectively reduce the RCS value to improve the stealth capability. Typically, a certain scattering direction is determined by theta and phi in spherical coordinates, and the RCS value (σ) is calculated as follows:[2,17]

$$\sigma(\mathrm{dBm}^2) = 10\lg\left[\frac{4\pi S}{\lambda^2}\left|\frac{E_s}{E_i}\right|^2\right] \quad (8)$$

where S, λ, E_s and E_i are the area of the simulated plate, length of the incident electromagnetic waves, and electric field intensities of the accepting wave, respectively. To further verify the stealth capability of M@C-rGO in practical applications, the far-field response in RCS of the samples is simulated by the CST Studio Suite. In the 3D radar scattering signal plot as shown in Fig. 6a–d, the color change and radiation flap structure can reflect the scattering signal strength. It can be observed that the three plates covered with the samples show lower scattering signals than the pure PEC plates, indicating that the samples show a significant suppression of electromagnetic wave scattering. In particular, the scattering signals of the Cu@C-rGO coated plates are significantly weaker for Mn@C-rGO and Ni@C-rGO, which is consistent with their microwave absorption properties. Furthermore, in order to visualize the differences in radar scattering signals, Fig. 6e shows the 2D curves of RCS values at different detection angles from −90° to 90°. When the detection angle is 0°, the scattered signal is the strongest and the RCS value at 0° gradually decreases to −90° and 90° with several fluctuations. It is noted that the three plates coated with Mn@C-rGO, Ni@C-rGO and Cu@C-rGO have smaller RCS values than the pure PEC plate in the range of −90° to 90° detection angles. Notably, when the detection angle is 0°, the RCS values of PEC, Mn@C-rGO, Ni@C-rGO and Cu@C-rGO are −0.91, −11.69, −12.16 and −15.1 dB m^2, respectively. For comparing the dissipation ability of electromagnetic waves of different coatings, the RCS reduction for different detection angles is investigated by subtracting the RCS value of the PEC substrate. As shown in Fig. 6f, all coatings have the best electromagnetic wave dissipation performance at detection angle 0°, where the RCS reductions are 10.78, 11.25, and 14.19 dB m^2 for Mn@C-rGO, Ni@C-rGO and Cu@C-rGO, respectively. Therefore, the above results show that M@C-rGO can effectively suppress the scattering and reflection of electromagnetic waves from the surface of the PEC substrate, which has promising practical applications.

Therefore, based on the above analysis, the possible microwave absorption mechanism of the synthesized M@rGO aerogels is presented in Fig. 7, which can be described as follows. (1) Multiple reflection and scattering. The sublimation of ice crystals builds a unique 3D porous structure for the M@rGO aerogels, which facilitates multiple reflections and scattering of electromagnetic waves within it, thus promoting multiple attenuation of electromagnetic waves. (2) Conduction loss. The 3D conductive network formed by cross-linking between reduced graphene oxide nanosheets provides a transmission channel for electron migration and hopping, which can effectively accelerate the electron transfer rate. In the transmission process of electrons, the electric field energy will be converted into thermal energy, and then the attenuation of the electromagnetic wave takes place. Moreover, the high electrical conductivity of the material results in a high complex dielectric constant, which leads to the efficient absorption of low-frequency electromagnetic waves. (3) Polarization loss. The abundance of defects and polar functional groups in the composites facilitates the formation of polarization centers, which induces dipole polarization. Furthermore, under the action of alternating electromagnetic field, due to the difference in conductivity between the metal sphere and rGO, the high-density positive and negative charges tend to accumulate at the interface of the metal sphere and rGO, forming a double capacitance structure, which can produce interface polarization and improve the dielectric loss. (4) Magnetic loss. The magnetic metal microspheres can provide magnetic loss to the synthesized aerogel, especially the natural resonance at low-frequency.

3.2.3. Thermal insulation and anticorrosion performance of M@C-rGO aerogels. In order to adapt to complex and changing application environments, the long-term stability of

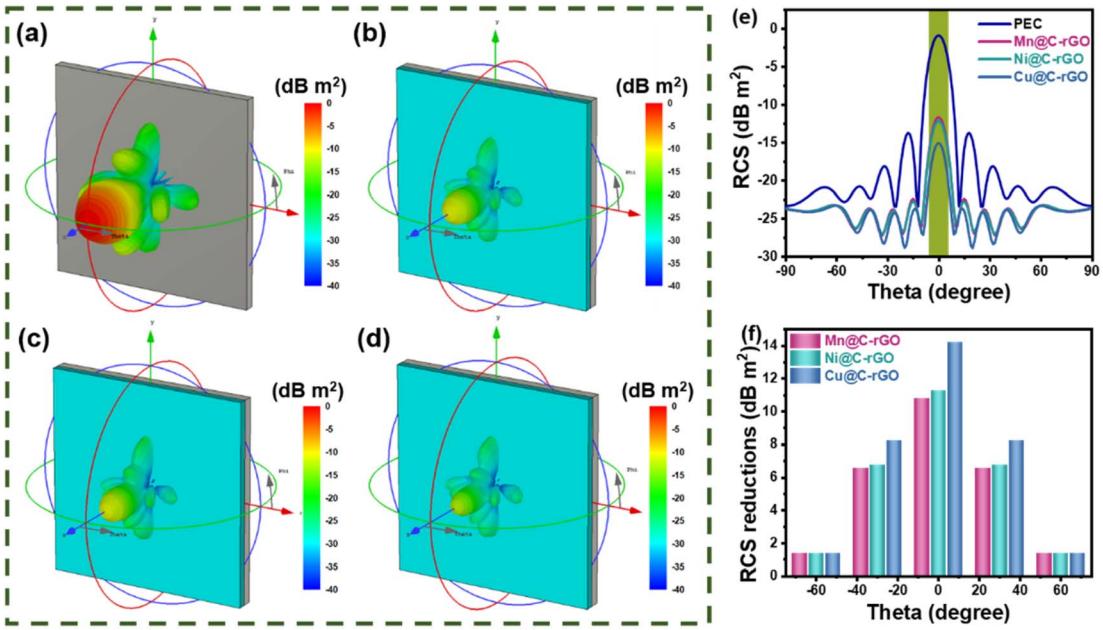

Fig. 6 The 3D radar wave scattering signals of (a) PEC, (b) Mn@C-rGO, (c) Ni@C-rGO and (d) Cu@C-rGO. (e) The simulated RCS curves of pure PEC and PEC coated with an absorber layer at different scanning angles. (f) The RCS value reduction *versus* pure PEC.

the microwave-absorbing material, including insulation and anticorrosion, is critical.[52] For characterizing the thermal insulation performance of M@rGO, the C-rGO, Mn@C-rGO, Ni@C-rGO and Cu@C-rGO with a thickness of about 10 mm are placed on a heat source at 90 °C, and the temperature changes on the upper surface are recorded using an infrared thermal imager, as shown in Fig. 8a–d. After heating for 5 min, the upper surface temperatures of the C-rGO, Mn@C-rGO, Ni@C-rGO and Cu@C-rGO are 42.0, 43.9, 44.6 and 45.1 °C, respectively. In addition, it can be observed from the side-view infrared image that the composite aerogel can prevent the upward heat conduction effectively, as in Fig. 8e. Typically, heat transfer is mainly through solid-phase heat conduction, gas-phase heat transfer and thermal radiation to transfer heat.

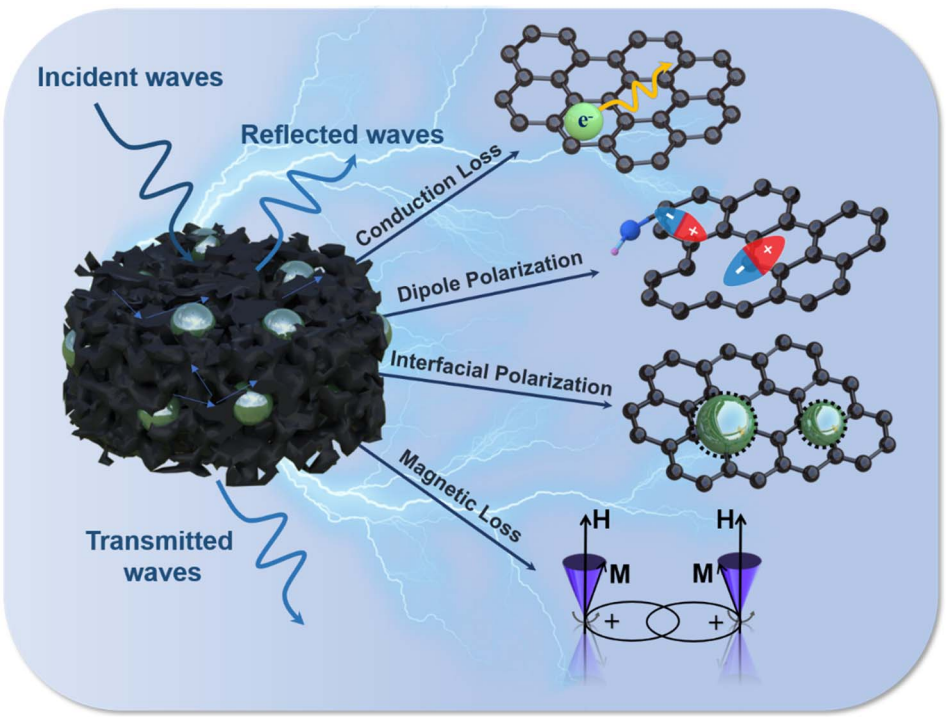

Fig. 7 Schematic illustration of microwave absorption mechanisms for the M@C-rGO.

The thermal conductivity of the composite aerogel is shown in Fig. 8f, large amounts of air within highly porous aerogels can significantly reduce the thermal conductivity and radiative heat transfer capacity of the solid phase. Also, the 3D porous structure can prolong the heat transfer channels and reduce the heat conductivity.[53,54]

Furthermore, the anticorrosive properties of the composite aerogel are investigated using electrochemical measurements with a three-electrode system in Fig. 9a. Generally, a higher open-circuit potential (OCP) indicates that the sample has a weak self-corrosion tendency.[55,56] As shown in Fig. 9b, the corrected OCP shows a trend of $OCP_{neutral}$ > $OCP_{alkaline}$ > OCP_{acid}, indicating that the samples show the strongest corrosion resistance under neutral conditions and the weakest under acidic conditions. Fig. 9c and d display the Tafel curves of composite aerogels in a neutral 3.5 wt% NaCl solution and the related corrosion parameters, including the corrosion voltage (E_{corr}) and the corrosion current (I_{corr}). Notably, the C-rGO, Mn@C-rGO, Ni@C-rGO and Cu@C-rGO demonstrate excellent anticorrosion ability due to their high E_{corr} values (1.65, 1.74, 1.73 and 1.61 V) and low I_{corr} values (2.88, 5.71, 4.68 and 3.55 μA). The fluctuations in OCP, E_{corr} and I_{corr} for different absorbers may be related to the activity of the inner metal microspheres. Moreover, the anticorrosion resistance of M@C-rGO can be further revealed by electrochemical impedance spectroscopy (EIS) measurement, as shown in Fig. 9e–g. The big radii of the capacitive arcs of the four absorbers in the Nyquist plots suggest their large charge transfer resistances. Typically, the impedance modulus at 0.01 Hz ($|Z|_{0.01\ Hz}$) is considered a semi-quantitative indicator for evaluating the system impedance and ability to shield corrosive media.[57] As shown in Fig. 9f, the $|Z|_{0.01\ Hz}$ values of the four samples reach 10^4 Ω cm^2 under neutral conditions, where C-rGO has the largest $|Z|_{0.01\ Hz}$ value of 7.52×10^4 Ω cm^2, indicating excellent anticorrosion properties. In addition, the high-frequency phase angle is a crucial indicator for evaluating the corrosion resistance of materials. The large high-frequency phase angle of the composite aerogels indicates their excellent anticorrosion properties (Fig. 9g).[58] To investigate further the corrosion mechanism, the EIS data are fitted using ZView software with the equivalent circuit of Fig. 9h, where R_s, R_c and R_{ct} represent the solution resistance, coating capacitance and charge transfer resistance, respectively, and Q_c and Q_{dl} are constant phase components. Generally, the R_{ct} value is a crucial indicator for evaluating the anticorrosion performance of materials.[59] Remarkably, the R_{ct} values of C-rGO, Mn@C-rGO, Ni@C-rGO and Cu@C-rGO are 5.841×10^5, 3.971×10^5, 2.885×10^5 and 1.421×10^5 Ω cm^2 respectively as shown in Table S2,† indicating that the synthesized aerogels have excellent corrosion resistance. Similarly, the samples also have superior corrosion resistance under acidic and alkaline conditions, as shown in Fig. S10 and S11.† Thus, the excellent corrosion resistance of synthetic aerogels is mainly attributed to the unique porous structure that can extend the penetration path of corrosive media through the "maze effect".[55]

In order to visually investigate the effect of corrosion on the microwave absorption performance of the samples, the samples are soaked in 3.5 wt% NaCl solution for 7 days. As shown in Fig. S12,† after 7 days of corrosion, the microwave absorption performance of the samples decreased but still demonstrated low-frequency absorption properties. Notably, all samples retained more than 90% of the EAB after corrosion. Therefore,

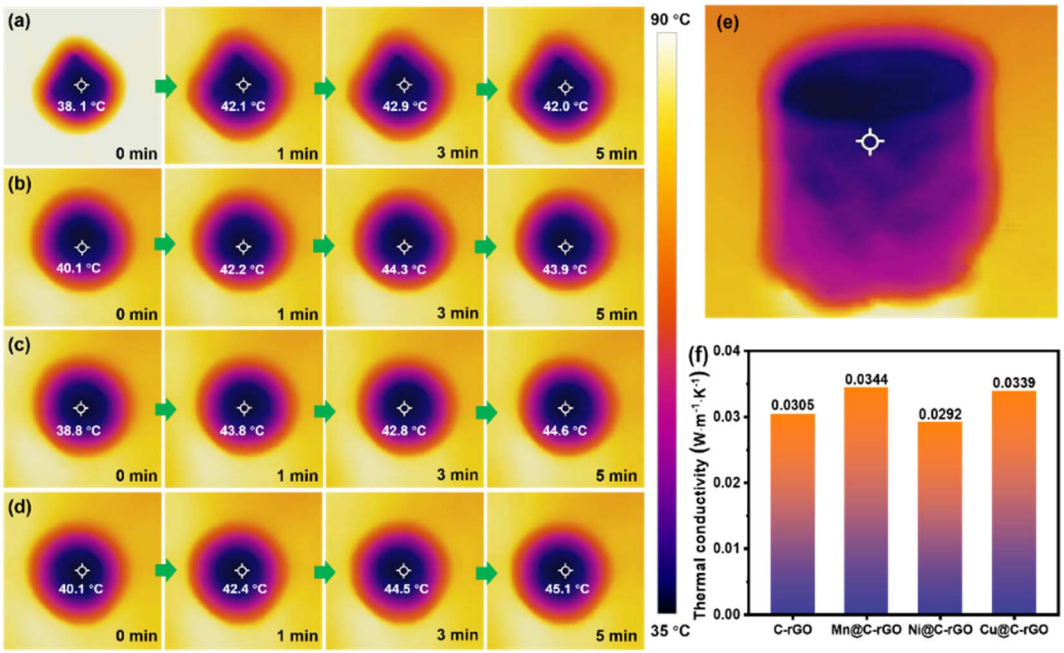

Fig. 8 The infrared images of (a) C-rGO, (b) Mn@C-rGO, (c) Ni@C-rGO and (d) Cu@C-rGO placed on the heat source at 90 °C. (e) The side-view infrared image of Cu@C-rGO and (f) thermal conductivity.

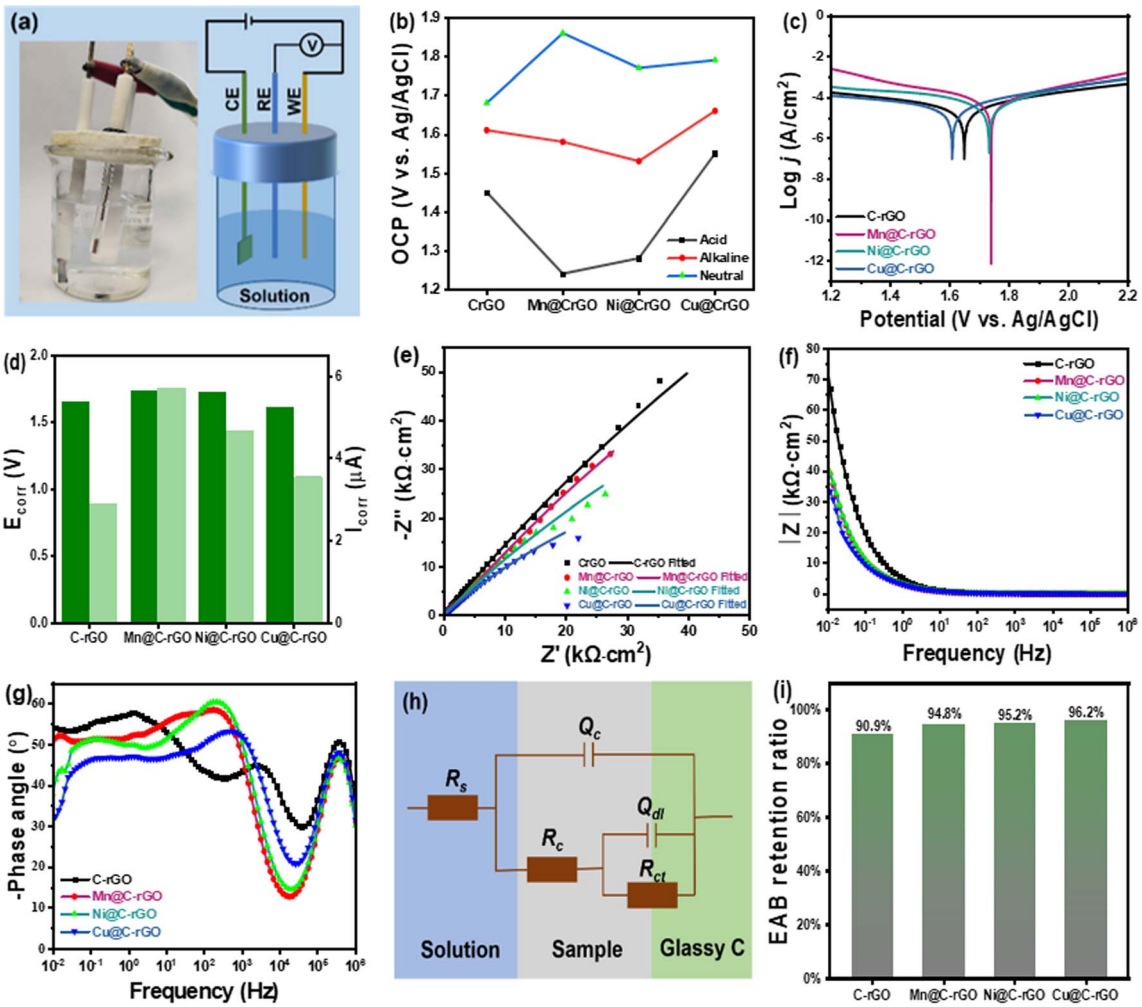

Fig. 9 (a) Schematic of the three-electrode system. (b) The OCP values under acidic, neutral, and alkaline environments. (c) The Tafel curves and (d) the E_{corr} and I_{corr} under neutral corrosion conditions. (e) The Nyquist plots, (f) Bode plots and (g) phase angle plots of four absorbers in neutral solutions. (h) The equivalent circuit and (i) the retained ratio of EAB after soaking in 3.5 wt% NaCl solution for 7 days.

excellent thermal insulation and anticorrosion protection properties favor the application of M@CrO aerogels in complex environments.

4. Conclusion

In summary, the M@C-rGO aerogel as a multifunctional nanomaterial was prepared *via* a facile ice template method and subsequent pyrolysis. Notably, the synthesized aerogels exhibit strong absorption in the low-frequency band and high-frequency band, where Mn@C-rGO, Ni@C-rGO, and Cu@C-rGO exhibit strong microwave absorption in the C-band with RL up to −53.42, −53.64 and −59.28 dB, respectively. More importantly, Mn@C-rGO, Ni@C-rGO, and Cu@C-rGO also have a wide EAB in the high-frequency band up to 6.16, 6.64 and 6.32 GHz, respectively. Moreover, the synthesized aerogels also exhibit superior radar stealth, thermal management and anticorrosion capability, wherein the thermal conductivities of Mn@C-rGO, Ni@C-rGO, and Cu@C-rGO are 0.0344, 0.0292 and 0.0339 W m^{-1} K^{-1}. Meanwhile, the R_{ct} values of Mn@C-rGO, Ni@C-rGO, and Cu@C-rGO are up to 3.971×10^5, 2.885×10^5 and 1.421×10^5 Ω cm^2, respectively. This work provides a new thought to design low-frequency microwave absorbers with good thermal management and anticorrosion capability. Also, it offers new insights into the preparation of a new generation of multifunctional materials in the field of microwave absorption, thermal insulation and anticorrosion, and the extended applications of the corresponding materials will be achieved.

Data availability

All data required to understand and verify the research in our manuscript have been made available on submission, and can be made available in this way, as part of the article (ESI),† or both.

Conflicts of interest

There are no conflicts to declare.

Acknowledgements

This work was financially supported by the National Natural Science Foundation of China (No. 52071009, 12011530067 and 11774020).

References

1 X. Li, D. Xu, D. Zhou, S. Pang, C. Du, M. A. Darwish, T. Zhou and S. K. Sun, Vertically Stacked Heterostructures of MXene/rGO Films with Enhanced Gradient Impedance for High-Performance Microwave Absorption, *Carbon*, 2023, **208**, 374–383.

2 X. Chen, Y. Li, S. Cheng, K. Wu, Q. Wang, L. Liu, F. Yang, A. Xie, H. Pang and C. Yu, Liquid Metal-MXene-Based Hierarchical Aerogel with Radar-Infrared Compatible Camouflage, *Adv. Funct. Mater.*, 2024, **34**, 2308274.

3 L. Wang, R. Mao, M. Huang, H. Jia, Y. Li, X. Li, Y. Cheng, J. Liu, J. Zhang, L. Wu and R. Che, Heterogeneous Interface Engineering Of High-Density MOFs-Derived Co Nanoparticles Anchored on N-Doped RGO toward Wide-Frequency Electromagnetic Wave Absorption, *Mater. Today Phys.*, 2023, **35**, 101128.

4 S. Wang, X. Zhang, S. Hao, J. Qiao, Z. Wang, L. Wu, J. Liu and F. Wang, Nitrogen-Doped Magnetic-Dielectric-Carbon Aerogel for High-Efficiency Electromagnetic Wave Absorption, *Nano-Micro Lett.*, 2024, **16**, 16.

5 H. Liu, Y. Yang, N. Tian, C. You and Y. Yang, Foam-Structured Carbon Materials and Composites for Electromagnetic Interference Shielding: Design Principles and Structural Evolution, *Carbon*, 2024, **217**, 118608.

6 H. Wei, W. Li and K. Bachagha, Component Optimization and Microstructure Design of Carbon Nanotube-Based Microwave Absorbing Materials: A review, *Carbon*, 2024, **217**, 118651.

7 X. Chen, Y. Li, S. Cheng, K. Wu, Q. Wang, L. Liu, F. Yang, A. Xie, H. Pang and C. Yu, Liquid Metal-MXene-Based Hierarchical Aerogel with Radar-Infrared Compatible Camouflage, *Adv. Funct. Mater.*, 2024, **34**, 2308274.

8 Y. Guo, Y. Duan, X. Liu, H. Zhang, T. Yuan, N. Wen, C. Li, H. Pan, Z. Fan and L. Pan, Boosting Conductive Loss and Magnetic Coupling Based on "Size Modulation Engineering" toward Lower-Frequency Microwave Absorption, *Small*, 2023, **20**, 2308809.

9 M. Yuan, H. Lv, H. Cheng, B. Zhao, G. Chen, J. Zhang and R. Che, Atomic and Electronic Reconstruction in Defective 0 D Molybdenum Carbide Heterostructure for Regulating Lower-Frequency Microwaves, *Adv. Funct. Mater.*, 2023, **33**, 2302003.

10 Z. Li, H. Zhu, L. Rao, M. Huang, Y. Qian, L. Wang, Y. Liu, J. Zhang, Y. Lai and R. Che, Wrinkle Structure Regulating Electromagnetic Parameters in Constructed Core–shell $ZnFe_2O_4$@PPy Microspheres as Absorption Materials, *Small*, 2024, **20**, 2308581.

11 J. Xiao, B. Zhan, M. He, X. Qi, X. Gong, J. Yang, Y. Qu, J. Ding, W. Zhong and J. Gu, Interfacial Polarization Loss Improvement Induced by the Hollow Engineering of Necklace-like PAN/Carbon Nanofibers for Boosted Microwave Absorption, *Adv. Funct. Mater.*, 2024, 2316722.

12 Q. Su, Y. He, D. Liu, K. Jia, L. Xia, X. Huang and B. Zhong, Facile Fabrication of Ultra-Light N-Doped-rGO/g-C_3N_4 for Broadband Microwave Absorption, *J. Colloid Interface Sci.*, 2023, **650**, 47–57.

13 C. Wu, Z. Chen, M. Wang, X. Cao, Y. Zhang, P. Song, T. Zhang, X. Ye, Y. Yang, W. Gu, J. Zhou and Y. Huang, Confining Tiny MoO_2 Clusters into Reduced Graphene Oxide for Highly Efficient Low Frequency Microwave Absorption, *Small*, 2020, **16**, 2001686.

14 J. Zhou, F. Guo, J. Luo, G. Hao, G. Liu, Y. Hu, G. Zhang, H. Guo, H. Zhou and W. Jiang, Designed 3D Heterostructure with 0D/1D/2D Hierarchy for Low-Frequency Microwave Absorption in the S-band, *J. Mater. Chem. C*, 2022, **10**, 1470–1478.

15 L. Chang, Y. Wang, X. Zhang, L. Li, H. Zhai and M. Cao, Toward High Performance Microwave Absorber by Implanting $La_{0.8}CoO_3$ Nanoparticles on rGO, *J. Mater. Sci. Technol.*, 2024, **174**, 176–187.

16 S. Wu, D. Chen, W. Han, Y. Xie, G. Zhao, S. Dong, M. Tan, H. Huang, S. Xu, G. Chen, Y. Cheng and X. Zhang, Ultralight and Hydrophobic Mxene/Chitosan-Derived Hybrid Carbon Aerogel with Hierarchical Pore Structure for Durable Electromagnetic Interference Shielding and Thermal Insulation, *Chem. Eng. J.*, 2022, **446**, 137093.

17 L. Rao, L. Wang, C. Yang, R. Zhang, J. Zhang, C. Liang and R. Che, Confined Diffusion Strategy for Customizing Magnetic Coupling Spaces to Enhance Low-frequency Electromagnetic Wave Absorption, *Adv. Funct. Mater.*, 2023, **33**, 2213258.

18 C. Zheng, M. Ning, Z. Zou, G. Lv, Q. Wu, J. Hou, Q. Man and R. Li, Two Birds with One Stone: Broadband Electromagnetic Wave Absorption and Anticorrosion Performance in 2-18 GHz for Prussian Blue Analog Derivatives Aimed for Practical Applications, *Small*, 2023, **19**, 2208211.

19 J. Li, Q. Wu, X. Wang, B. Wang and T. Liu, Metal-Organic Framework-Derived Co/Coo Nanoparticles with Tunable Particle Size for Strong Low-Frequency Microwave Absorption in the S and C Bands, *J. Colloid Interface Sci.*, 2022, **628**, 10–21.

20 L. Rao, L. Wang, C. Yang, R. Zhang, J. Zhang, C. Liang and R. Che, Confined Diffusion Strategy for Customizing Magnetic Coupling Spaces to Enhance Low-Frequency Electromagnetic Wave Absorption, *Adv. Funct. Mater.*, 2023, **33**, 2213258.

21 M. Ling, P. Liu, F. Wu and B. Zhang, Three-dimensional RGO/CNTs/GDY Assembled Microsphere: Bridging-Induced Electron Transport Enhanced Microwave Absorbing Mechanism, *Carbon*, 2023, **214**, 118351.

22 H. Liu, Y. Yang, N. Tian, C. You and Y. Yang, Foam-Structured Carbon Materials and Composites for Electromagnetic Interference Shielding: Design Principles and Structural Evolution, *Carbon*, 2024, **217**, 118608.

23 X. Xu, S. Shi, Y. Tang, G. Wang, M. Zhou, G. Zhao, X. Zhou, S. Lin and F. Meng, Growth of NiAl-Layered Double Hydroxide on Graphene toward Excellent Anticorrosive

Microwave Absorption Application, *Adv. Sci.*, 2021, **8**, 2002658.

24 J. Yao, J. Zhou, L. Lu, F. Yang, Z. Yao, B. Ouyang, E. Kan, Y. Zuo, R. Che and F. Wu, Rare Earth Lanthanum Pinning Effect for Corrosion Resistance Ultraefficient Microwave Absorption FeCo@rGO Composites, *J. Mater. Sci. Technol.*, 2024, **177**, 181–190.

25 L. Yao, Y. Wang, J. Zhao, Y. Zhu and M. Cao, Multifunctional Nanocrystalline-Assembled Porous Hierarchical Material and Device for Integrating Microwave Absorption, Electromagnetic Interference Shielding, and Energy Storage, *Small*, 2023, **19**, 2208101.

26 J. Zhang, L. Chen, X. Li, H. Cao, W. Chen and X. Wang, Regulation Dipole Moments of N-Doped Graphene Coordinated with FePc Toward Highly Efficient Microwave Absorption Performance in C Band, *Small*, 2024, 2308459.

27 Z. Tang, L. Xu, C. Xie, L. Guo, L. Zhang, S. Guo and J. Peng, Synthesis of $CuCo_2S_4$@Expanded Graphite with Crystal/Amorphous Heterointerface and Defects for Electromagnetic Wave Absorption, *Nat. Commun.*, 2023, **14**, 5951.

28 H. Jin, J. Zhou, J. Tao, Y. Gu, C. Yu, P. Chen and Z. Yao, Commonly Neglected Ester Groups Enhanced Microwave Absorption, *Small*, 2023, **19**, 2304536.

29 J. Qiu, C. Peng, R. Wang, C. Yao, X. Liu, Q. Wang and W. Wang, One-step In-Situ Preparation Of C/TiO_2@rGO Aerogel Derived from Ti_3C_2T MXene for Integrating Microwave Absorption, Electromagnetic Interference Shielding and Catalytic Degradation of Antibiotics, *Carbon*, 2024, **217**, 118610.

30 C. Peng, R. Wang, C. Yao, J. Qiu, X. Liu, Q. Wang and W. Wang, Nest-like Hollow Cu-Doped Co/CoO/C Microspheres Derived from Spherical Co-ZIF with Controllable Microwave Absorption Performance, *Appl. Surf. Sci.*, 2023, **641**, 158496.

31 Z. L. Hou, X. Gao, J. Zhang and G. Wang, A Perspective On Impedance Matching and Resonance Absorption Mechanism for Electromagnetic Wave Absorbing, *Carbon*, 2024, **222**, 118935.

32 D. Yang, S. Dong, T. Cui, J. Xin, X. Xu, J. Chen, Y. Xie, G. Chen, C. Hong and X. Zhang, Multifunctional Carbon Fiber Reinforced C/SiOC Aerogel Composites for Efficient Electromagnetic Wave Absorption, Thermal Insulation, and Flame Retardancy, *Small*, 2023, 2308145.

33 T. Zhu, S. Chang, Y. F. Song, M. Lahoubi and W. Wang, PVP-Encapsulated $CoFe_2O_4$/rGO Composites with Controllable Electromagnetic Wave Absorption Performance, *Chem. Eng. J.*, 2019, **373**, 755–766.

34 M. Qin, L. Zhang, X. Zhao and H. Wu, Defect Induced Polarization Loss in Multi-Shelled Spinel Hollow Spheres for Electromagnetic Wave Absorption Application, *Adv. Sci.*, 2021, **8**, 2004640.

35 T. Zhu, W. Shen, X. Wang, Y. F. Song and W. Wang, Paramagnetic CoS_2@MoS_2 Core–Shell Composites Coated by Reduced Graphene Oxide as Broadband and Tunable High-Performance Microwave Absorbers, *Chem. Eng. J.*, 2019, **378**, 122159.

36 X. Wang, J. Liao, R. Du, G. Wang, N. Tsidaeva and W. Wang, Achieving Super-Broad Effective Absorption Bandwidth with Low Filler Loading for Graphene Aerogels/Raspberry-Like $CoFe_2O_4$ Clusters by N Doping, *J. Colloid Interface Sci.*, 2021, **590**, 186–198.

37 P. Liu, Y. Zhang, J. Yan, Y. Huang, L. Xia and Z. Guang, Synthesis of Lightweight N-Doped Graphene Foams with Open Reticular Structure for High-Efficiency Electromagnetic Wave Absorption, *Chem. Eng. J.*, 2019, **368**, 285–298.

38 J. Qiu, H. Cao, J. Liao, R. Du, K. Dou, N. Tsidaeva and W. Wang, 3D Porous Coral-Like $Co_{1.29}Ni_{1.71}O_4$ Microspheres Embedded into Reduced Graphene Oxide Aerogels with Lightweight and Broadband Microwave Absorption, *J. Colloid Interface Sci.*, 2022, **609**, 12–22.

39 F. Zhang, S. Shang, Y. Li, B. Fan, R. Zhang, B. Zhao, H. Lu and C. Ma, Tunable Electromagnetic Properties of $Ti_3C_2T_x$/rGO Foams Decorated with NiO Particles, *CrystEngComm*, 2022, **24**, 5949–5957.

40 T. Hou, J. Wang, T. Zheng, Y. Liu, G. Wu and P. Yin, Anion Exchange of Metal Particles on Carbon-Based Skeletons for Promoting Dielectric Equilibrium and High-Efficiency Electromagnetic Wave Absorption, *Small*, 2023, **19**, 2303463.

41 M. Ling, F. Ge, F. Wu, L. Zhang, Q. Zhang and B. Zhang, Effect of Crystal Transformation on the Intrinsic Defects and the Microwave Absorption Performance of $Mo_2TiC_2T_x$/RGO Microspheres, *Small*, 2024, **20**, 2306233.

42 M. Yuan, B. Zhao, C. Yang, K. Pei, L. Wang, R. Zhang, W. You, X. Liu, X. Zhang and R. Che, Remarkable Magnetic Exchange Coupling *via* Constructing Bi–Magnetic Interface for Broadband Lower-Frequency Microwave Absorption, *Adv. Funct. Mater.*, 2022, **32**, 2203161.

43 C. Wang, Y. Feng, J. Zhou, G. Wen and L. Xia, Numerical Analysis, Experimental Verification and Criterion Establishment of Non-Magnetic Microwave Absorbing Material, *J. Colloid Interface Sci.*, 2022, **613**, 256–264.

44 L. Guo, Q. D. An, Z. Y. Xiao, S. R. Zhai and L. Cui, Inherent N-Doped Honeycomb-like Carbon/Fe_3O_4 Composites with Versatility for Efficient Microwave Absorption and Wastewater Treatment, *ACS Sustain. Chem. Eng.*, 2019, **7**, 9237–9248.

45 X. Wang, Y. Lu, T. Zhu, S. Chang and W. Wang, $CoFe_2O_4$/N-Doped Reduced Graphene Oxide Aerogels for High-Performance Microwave Absorption, *Chem. Eng. J.*, 2020, **388**, 124317.

46 X. Wang, T. Zhu, S. Chang, Y. Lu, W. Mi and W. Wang, 3D Nest-Like Architecture of Core–Shell $CoFe_2O_4$@1T/2H-MoS_2 Composites with Tunable Microwave Absorption Performance, *ACS Appl. Mater. Interfaces*, 2020, **12**, 11252–11264.

47 T. Yu, J. Qiu, J. Liao, X. Wang, W. Chen, Y. Cheng, W. Wang and Y. F. Song, Topological Transformation Strategy for Layered Double Hydroxide@Carbon Nanofibers as Highly Efficient Electromagnetic Wave Absorber, *J. Alloys Compd.*, 2021, **867**, 159046.

48 F. Hu, H. Tang, F. Wu, P. Ding, P. Zhang, W. Sun, L. Cai, B. Fan, R. Zhang and Z. Sun, Sn Whiskers from Ti_2SnC

Max Phase: Bridging Dual-Functionality in Electromagnetic Attenuation, *Small Methods*, 2024, 2301476.

49 J. Qiu, J. Liao, G. Wang, R. Du, N. Tsidaeva and W. Wang, Implanting N-doped CQDs into rGO Aerogels With Diversified Applications in Microwave Absorption and Wastewater Treatment, *Chem. Eng. J.*, 2022, **443**, 136475.

50 C. Peng, H. Cao, R. Wang, J. Qiu and W. Wang, Construction of ZIF/CS and ZIF/CS-Derivatives with High-Efficiency Adsorption for Dyes/Antibiotics and Strong Microwave Absorption Performance, *Colloids Surf., A*, 2004, **695**, 134210.

51 F. Pan, K. Pei, G. Chen, H. Guo, H. Jiang, R. Che and W. Lu, Integrated Electromagnetic Device with On–Off Heterointerface for Intelligent Switching Between Wave-Absorption and Wave-Transmission, *Adv. Funct. Mater.*, 2023, **33**, 2306599.

52 Z. Zhao, D. Lan, L. Zhang and H. Wu, A Flexible, Mechanically Strong, and Anti-Corrosion Electromagnetic Wave Absorption Composite Film with Periodic Electroconductive Patterns, *Adv. Funct. Mater.*, 2022, **32**, 2111045.

53 L. Cai, H. Jiang, F. Pan, H. Liang, Y. Shi, X. Wang, J. Cheng, Y. Yang, X. Zhang, Z. Shi, H. Wu and W. Lu, Linkage Effect Induced by Hierarchical Architecture in Magnetic MXene-based Microwave Absorber, *Small*, 2024, **20**, 2306698.

54 F. Wu, P. Hu, F. Hu, Z. Tian, J. Tang, P. Zhang, L. Pan, M. Barsoum, L. Cai and Z. Sun, Multifunctional MXene/C Aerogels for Enhanced Microwave Absorption and Thermal Insulation, *Nano-Micro Lett.*, 2023, **15**, 194.

55 C. Zheng, M. Ning, Z. Zou, G. Lv, Q. Wu, J. Hou, Q. Man and R. Li, Two Birds with One Stone: Broadband Electromagnetic Wave Absorption and Anticorrosion Performance in 2-18 GHz for Prussian Blue Analog Derivatives Aimed for Practical Applications, *Small*, 2023, **19**, 2208211.

56 J. Xiao, B. Zhan, M. He, X. Qi, X. Gong, J. Yang, Y. Qu, J. Ding, W. Zhong and J. Gu, Interfacial Polarization Loss Improvement Induced by the Hollow Engineering of Necklace-like PAN/Carbon Nanofibers for Boosted Microwave Absorption, *Adv. Funct. Mater.*, 2024, 2316722.

57 S. Chen, Y. Meng, X. Wang, D. Liu, X. Meng, X. Wang and G. Wu, Hollow tubular MnO_2/MXene (Ti_3C_2, Nb_2C, and V_2C) Composites as High-Efficiency Absorbers with Synergistic Anticorrosion Performance, *Carbon*, 2024, **218**, 118698.

58 Y. Zhang, L. Zhang, L. Tang, R. Du and B. Zhang, S-NiSe/HG Nanocomposites with Balanced Dielectric Loss Encapsulated in Room-Temperature Self-Healing Polyurethane for Microwave Absorption and Corrosion Protection, *ACS Nano*, 2024, **18**, 8411–8422.

59 K. Li, L. Han, X. Wang, F. Gao, J. Zhang and J. Cheng, MOF-derived CoNC@rGO/Amine-Rich@rGO/Fluorinated-Epoxy Nanocomposites with EMI Shielding, Mechanical Robustness, Superamphiphobicity and Long-Term Anticorrosion Properties, *Chem. Eng. J.*, 2023, **455**, 140542.